LoCuSS : The Splashback Radius of Massive Galaxy Clusters and Its Dependence on Cluster Merger History

Bianconi, Matteo

2021-04

acceptedVersion

LoCuSS: The splashback radius of massive galaxy clusters and its dependence on cluster merger history

Matteo Bianconi,[1] Riccardo Buscicchio,[1,2] Graham P. Smith,[1] Sean L. McGee,[1] Chris P. Haines,[3] Alexis Finoguenov,[4] and Arif Babul[5]

[1]School of Physics & Astronomy, University of Birmingham, Birmingham, B15 2TT, UK
[2]Institute for Gravitational Wave Astronomy, University of Birmingham, Birmingham, B15 2TT, UK
[3]Instituto de Astronomía y Ciencias Planetarias de Atacama, Universidad de Atacama, Copayapu 485, Copiapó, Chile
[4]Department of Physics, University of Helsinki, Gustaf Hällströmin katu 2a, FI-0014 Helsinki, Finland
[5]Department of Physics and Astronomy, University of Victoria, Victoria, BC V8P 1A1, Canada

Abstract

We present the direct detection of the splashback feature using the sample of massive galaxy clusters from the Local Cluster Substructure Survey (LoCuSS). This feature is clearly detected (above 5σ) in the stacked luminosity density profile obtained using the K-band magnitudes of spectroscopically confirmed cluster members. We obtained the best-fit model by means of Bayesian inference, which ranked models including the splashback feature as more descriptive of the data with respect to models that do not allow for this transition. In addition, we have assessed the impact of the cluster dynamical state on the occurrence of the splashback feature. We exploited the extensive multi-wavelength LoCuSS dataset to test a wide range of proxies for the cluster formation history, finding the most significant dependence of the splashback feature location and scale according to the presence or absence of X-ray emitting galaxy groups in the cluster infall regions. In particular, we report for the first time that clusters that do not show massive infalling groups present the splashback feature at a smaller clustercentric radius $r_{\rm sp}/r_{200,\rm m} = 1.158 \pm 0.071$ than clusters that are actively accreting groups $r_{\rm sp}/r_{200,\rm m} = 1.291 \pm 0.062$. The difference between these two sub-samples is significant at 4.2σ, suggesting a correlation between the properties of the cluster potential and its accretion rate and merger history. Similarly, clusters that are classified as old and dynamically inactive present stronger signatures of the splashback feature, with respect to younger, more active clusters. We are directly observing how fundamental dynamical properties of clusters reverberate across vastly different physical scales.

1. INTRODUCTION

The outskirts of galaxy clusters are the new frontier to improve our understanding of the multi-faceted physical processes impacting baryons and dark matter during structure formation. They mark the transition between pristine field sparseness and evolved collapsed haloes. Here merger shocks are produced and galaxy evolution is jolted, due to accretion on to clusters (Walker et al. 2019). This makes cluster outskirts the prime targets to observe the transformation of

Corresponding author: Matteo Bianconi
mbianconi@star.sr.bham.ac.uk

galaxy properties (Haines et al. 2015), to assess biases in clusters mass estimates (Reiprich et al. 2013), and test predictions of cosmological models (Pratt et al. 2019).

The collapse and growth of dark matter haloes follows the evolution of primordial density perturbations whose gravitational pull locally overcomes the expansion of the Universe. In the simplest scenario involving spherically-symmetric, continuous accretion, virialization during collapse redistributes the potential energy of the primordial overdensities, allowing for a final stable structure characterised by a specific density contrast $\Delta_{\rm vir}$ (Gunn & Gott 1972, see also Voit 2005 for a review). It follows that the mass enclosed within the virialized sphere is $M_{\rm vir} = \frac{4}{3}\pi r_{\rm vir}^3 \Delta_{\rm vir}\bar{\delta}$ (Cole & Lacey 1996). This definition is commonly used to indicate
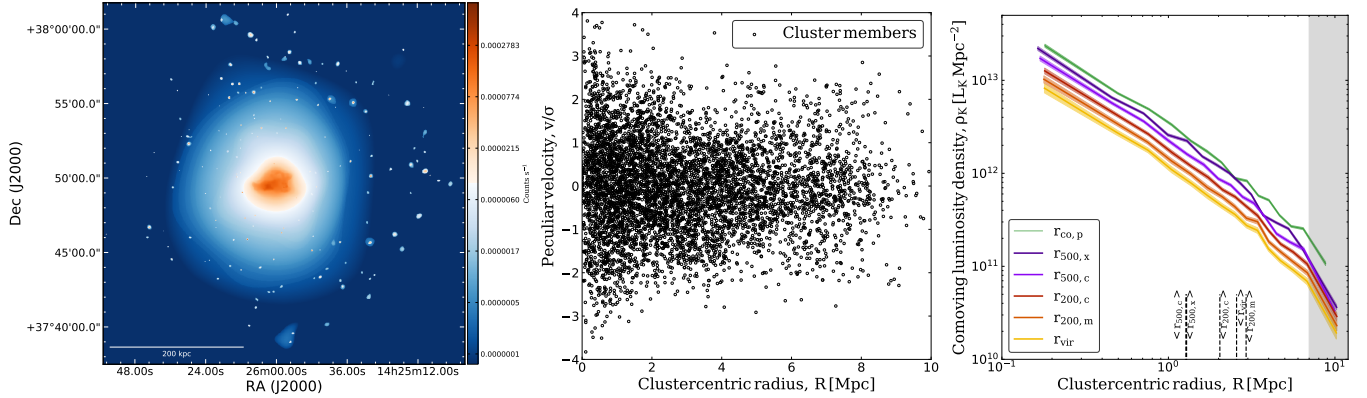
Figure 1. Left panel: X-ray emission counts s^{-1}, tracing the diffuse hot intracluster medium which permeates the central region of cluster Abell 1914, and individual emission from active galactic nuclei, observed using the *Chandra* telescope. Middle panel: stacked phase-space diagram of the cluster members selected following the procedure outlined in Section 2. The clustercentric radius of spectroscopically confirmed cluster members of 20 LoCuSS clusters is plotted with respect to their peculiar velocity relative to the central redshift of the their host cluster, scaled by the velocity dispersion of all the cluster members within r_{200}. The peculiar velocity of each galaxies is computed as following $v_{gal} = c \times (z_{gal} - z_{halo})/(1 + z_{halo})$, where z_{gal} and z_{halo} are the galaxy and its parent halo redshift. Right panel: comoving luminosity density of LoCuSS cluster galaxies, plotted with respect to comoving clustercentric radius. The individual profiles refer to different density threshold scaling, and are artificially offset vertically for viewing purposes except for the profile labelled $r_{500,c}$. The profile labelled $r_{co,p}$ marks the luminosity profile without any scaling. The values of $r_{500,c}$ and $r_{500,x}$ are computed using ΛCDM cosmology (Martino et al. 2014; Okabe & Smith 2016), and are displayed solely for comparison. The grey shaded area marks the radial completeness threshold defined in Section 2.

gravitationally bound structures, while allowing for different choices of $\Delta \in [180, 200, 500]$ and reference density $\bar{\delta}$, namely the mean matter density or critical density of the Universe. This formalism is particularly advantageous since it permits a bridge between simulations and observations, and it has been used to probe self-similarity for a wide range of halo properties, involving both baryonic and non-baryonic matter, in regimes that are dominated by gravity (e.g. Navarro et al. 1996; Bullock et al. 2001; Tinker et al. 2008; Schaller et al. 2015; Springel et al. 2018; Farahi et al. 2019).

Modifications have been proposed to the idealized collapse model to allow for more general conditions of structure growth, such as those in ΛCDM cosmology (Bryan & Norman 1998). However, it is a challenge to fully describe the structure on the outskirts of these halos, with models generally unable to capture the rich extent of density fields that connect haloes which are gravitationally bound despite being separated by many virial radii (Prada et al. 2006). Indeed, as the density contrast is defined against mean cosmic densities which have a redshift dependence, an intrinsic pseudo-evolution of halo masses arises from the formalism (Babul et al. 2002; Diemand et al. 2007; Diemer et al. 2013). Naively, the spherical collapse model suggests the presence of a sharp transition in the radial density profile of the forming halo, corresponding to the region which physically separates gravitationally bound matter accreted previously from newly-infalling regions (Fillmore & Goldreich 1984; Bertschinger 1985; Adhikari et al. 2014; Shi 2016). Infalling particles which get trapped in the growing halo potential populate a shell at the apocenter of their first orbit – the so-called splashback region. For this

reason, the splashback radius has been proposed as physical boundary of collapsed haloes and is detected as a steepening of the radial density profile of dark matter halos from large-scale numerical simulations (Diemer & Kravtsov 2014; More et al. 2015, see also Tomooka et al. 2020).

Observationally, the challenge of detecting the splashback radius has been recently undertaken using galaxies and gas measured in large-scale surveys as tracers of the underlying dark matter halo potential in galaxy clusters. Unfortunately, it has become apparent that the measured splashback radius can be significantly affected by the cluster selection method. Optical selection methods based on cluster richness measured within an aperture result in an underestimated splashback location due to projection effects and interloper contamination (Zu et al. 2017; Busch & White 2017; Baxter et al. 2017). Additional biases on the measure of the splashback location have been confirmed for methods relying on clusters selected using redMaPPer (Rykoff et al. 2014) by comparison with cluster mass profiles obtained using weak-lensing shear (Chang et al. 2018). More recently, selection methods which are unaffected by the same biases, and thus minimize the risk of spurious correlations between the splashback radius and the cluster selection, such as Sunyaev-Zel'dovich (SZ, Sunyaev & Zeldovich 1972) (Shin et al. 2019; Zürcher & More 2019; Adhikari et al. 2020) and X-ray (Umetsu & Diemer 2017), have been attempted. To date, these methods have yielded less precise measurements of the splashback radius due to their smaller samples (More et al. 2015; Baxter et al. 2017; Murata et al. 2020), and to the typically noisy measurements from weak-lensing at these radii.

Table 1. List of clusters selected for this study, presented together with central coordinates, average redshift, weak-lensing mass $M_{200,\mathrm{m}}$ from Okabe & Smith (2016), and membership of the main sub-samples discussed in the text, and based on Haines et al. (2018) and Sanderson et al. (2009).

Name	RA(J2000)	Dec(J2000)	Redshift $\langle z \rangle$	$M_{200,\mathrm{m}}$ $10^{14}h^{-1}M_\odot$	Infalling groups?	Low entropy core?
Abell 68	00:37:06.84	+09:09:24.28	0.251	$8.39^{+2.00}_{-1.64}$	Y	N
ZwCl 0104.4+0048	01:06:49.50	+01:03:22.10	0.253	$2.98^{+2.21}_{-1.26}$	N	Y
Abell 209	01:31:53.45	−13:36:47.84	0.209	$17.01^{+3.70}_{-2.93}$	Y	N
Abell 383	02:48:03.42	−03:31:45.05	0.189	$6.90^{+2.18}_{-1.64}$	N	Y
Abell 586	07:32:20.22	+31:37:55.88	0.171	$8.32^{+3.54}_{-2.32}$	N	N
Abell 611	08:00:56.81	+36:03:23.40	0.286	$11.77^{+2.77}_{-2.35}$	Y	N
Abell 697	08:42:57.58	+36:21:59.54	0.282	$14.22^{+6.14}_{-3.73}$	Y	N
ZwCl 0857.9+2107	09:00:36.86	+20:53:39.84	0.234	$3.52^{+1.97}_{-1.39}$	N	Y
Abell 963	10:17:03.65	+39:02:49.63	0.204	$9.46^{+2.20}_{-1.79}$	Y	Y
Abell 1689	13:11:29.45	−01:20:28.32	0.185	$13.15^{+2.32}_{-1.97}$	N	N
Abell 1758	13:32:33.50	+50:30:31.61	0.279	$7.22^{+2.42}_{-1.83}$	Y	N
Abell 1763	13:35:18.07	+40:59:57.16	0.232	$22.89^{+5.94}_{-4.32}$	Y	N
Abell 1835	14:00:52.50	+02:52:42.64	0.252	$12.27^{+2.75}_{-2.28}$	Y	Y
Abell 1914	14:25:59.70	+37:49:41.63	0.167	$12.51^{+3.55}_{-2.65}$	Y	N
ZwCl 1454.8+2233	14:57:15.11	+22:20:34.26	0.257	$6.28^{+6.10}_{-2.69}$	Y	Y
Abell 2219	16:40:22.56	+46:42:21.60	0.226	$15.17^{+4.53}_{-3.16}$	Y	N
RXJ 1720.1+2638	17:20:10.14	+26:37:30.90	0.160	$7.23^{+3.46}_{-2.26}$	Y	Y
RXJ 2129.6+0005	21:29:39.88	+00:05:20.54	0.234	$7.35^{+4.11}_{-2.48}$	N	Y
Abell 2390	21:53:36.85	+17:41:43.66	0.229	$13.75^{+2.91}_{-2.42}$	Y	Y
Abell 2485	22:48:31.13	−16:06:25.60	0.247	$7.56^{+2.27}_{-1.74}$	N	N

Simulations indicate that cluster outskirts are continuously bombarded by smaller haloes, galaxy- or group-like, which is the prevalent ingredient for the fast evolution of cluster mass, especially below redshift $z < 0.5$ (McGee et al. 2009; De Lucia et al. 2012). The overall mass accretion rate is shown to impact the measured cluster density profiles. In particular, high accretion rates translate in to steep slopes of the density profiles, even in projection at radii $r > 0.5\,R_{200,\mathrm{m}}$ (Diemer & Kravtsov 2014). In addition, fast accretion impacts clusters across their entire extent, inducing rapid growth in both r_s and r_{500}, with respect to quieter clusters whose inner regions remain undisturbed while still accreting mass in their outskirts (Mostoghiu et al. 2019). Confirmation of this ongoing accretion is given from the increasing efforts of observations to census infalling haloes at their first encounter with the cluster potential, such as ram-pressure stripped galaxies (Poggianti et al. 2016) and groups (Eckert et al. 2014). Therefore, a systematic cluster campaign targeting infalling haloes enables simultaneously to address galaxy evolution, cluster physics and physics of hierarchical assembly (e.g. Haines et al. 2018; Bianconi et al. 2018). An observational study of a well-defined cluster sample that would enable direct comparison

with theoretical predictions of the impact of merger history on the splashback feature has not been attempted so far.

In this work, we present the detection of the splashback feature in a sample of massive X-ray selected clusters at redshifts of $0.15 < z < 0.3$ selected from the Local Cluster Substructure Survey (LoCuSS). Specifically, we take advantage of the rich multi-wavelength LoCuSS dataset and highly complete spectroscopic follow-up observations from the Arizona Cluster Redshift Survey (ACReS) to detect the feature in stacked projected density profile of the clusters, constrain the de-projected splashback radius of the whole sample, and examine how the splashback radius depends on observables that probe the assembly history of the clusters. The use of spectroscopically-confirmed cluster member galaxies, and dissection of the cluster sample based on their properties, are important new steps that can help to shape future investigations of cluster assembly with upcoming surveys including the Vera Rubin Observatory's Legacy Survey of Space and Time, ESA's *Euclid* satellite, ESO's 4MOST instrument, and the German-Russian *eROSITA* X-ray satellite.

In Section 2 we define the cluster sample, give an overview of the LoCuSS/ACReS dataset, and discuss the structure of the

Table 2. Guide to the LoCuSS datasets used in this article. The references listed in the final column are as follows: 1. Martino et al. (2014); 2. Okabe & Smith (2016); 3. Haines et al. (2018); 4. Bianconi et al. (2018); 5. Sanderson et al. (2009); 6. Mulroy et al. (2019).

Telescope:	*XMM-Newton*	*Chandra*	Subaru	MMT	UKIRT	
Instrument:	EPIC	ACIS-I	SuprimeCAM	Hectospec	WFCAM	
Energy / wavelength:	0.5-2.4 keV	0.3-7 keV	V/i'-bands	$400-900$nm	J/K-bands	
Physical radius probed:	$1.5r_{200,m}$	$0.8r_{200,m}$	$1.5r_{200,m}$	$3r_{200,m}$	$2.5r_{200,m}$	
Sensitivity:	10^{-14} erg s^{-1} cm^{-2}	10^{-13} erg s^{-1} cm^{-2}	$V(5\sigma) = 27.5$	90% complete	$J(5\sigma) = 23$	
			$i'(5\sigma) = 26$	at $K \leq K^\star + 1.5$	$K(5\sigma) = 22$	
Measurements:	. . . . Datasets used					References
Density profile				✓	✓	This paper
Total cluster mass	✓	✓	✓			1, 2
Infalling groups	✓			✓	✓	3, 4
Central entropy	✓	✓				5
X-ray centroid shift	✓	✓				1
X-ray concentration	✓	✓				1
Luminosity gap			✓	✓	✓	6
X-ray / BCG offset	✓	✓		✓	✓	6

clusters in our sample. In Section 3, we describe the details of how we approach the modelling of the data. Section 4 contains our results, beginning with the empirical detection of the splashback feature in the stacked projected density profile of the clusters, before applying the Bayesian modeling scheme described in Section 3 to infer the splashback radius in 3-dimensions, and finally examining how the results depend on the structure of the clusters. We close by summarising and discussing our results in Section 5. We assume cosmology values presented in Planck Collaboration et al. (2016), with $h = 0.678$, $H_0 = 100\,h\,\mathrm{km\,s^{-1}\,Mpc^{-1}}$, $\Omega_m = 0.309$ and $\Omega_\Lambda = 0.691$.

2. SAMPLE, DATA AND CLUSTER PROPERTIES

The Local Cluster Substructure Survey (LoCuSS, PI: G. P. Smith) is a multiwavelength survey of X-ray selected massive galaxy clusters from the *ROSAT* All Sky Survey (Ebeling et al. 1998; Böhringer et al. 2004). We study 20 clusters that are the union of the complete high-L_X sample of 50 clusters (Okabe et al. 2013; Martino et al. 2014; Okabe & Smith 2016; Smith et al. 2016; Mulroy et al. 2019; Farahi et al. 2019), and the galaxy evolution sample of 30 clusters (Smith et al. 2010; Haines et al. 2012, 2013, 2015, 2018; Bianconi et al. 2018). Therefore, the sample of 20 clusters considered here are an unbiased sub-sample of the complete high-L_X sample, for which high quality wide-field multi-wavelength data are available. For reference, the high-L_X sample was selected using the following criteria: $0.15 \leq z \leq 0.3$, $L_X(0.1 - 2.4\mathrm{keV})/E(z) \geq 4.2 \times 10^{44}$ erg s^{-1}, and $-25 < \delta[\mathrm{deg}] < +65$, $n_H \leq 7 \times 10^{20}\mathrm{cm^{-2}}$. The 20 clusters are listed in Table 1.

The full wide-field multiwavelength dataset on the sample of 20 clusters spans X-ray to millimetre wavelengths, and includes data from *Chandra*, *XMM-Newton*, GALEX, the Subaru 8.2-m telescope, the Hectospec instrument on the Multiple Mirror Telescope (MMT), UKIRT/WFCAM, the Mayall 4-m telescope, *WISE*, *Spitzer*/MIPS, the PACS and SPIRE instruments on *Herschel*, the Sunyaev Zeldovich Array, and ESA's *Planck* satellite. We concentrate on the X-ray, optical, and near-infrared data in this article, and summarize the cluster properties derived from these data, and previously published LoCuSS articles that contain detailed information in Table 2.

Highly complete spectroscopic follow-up of stellar-mass selected candidate galaxy cluster member galaxies out to $\approx 3r_{200,m}$ from the Arizona Cluster Redshift Survey (ACReS[1]) is central to our analysis and results. This is because we aim to use spectroscopically confirmed member galaxies as test particles to measure the density profile of the clusters on scales well outside the physical scale on which the splashback feature is expected to be found. The combined UKIRT/WFCAM and MMT/Hectospec dataset allows us to do this to projected clustercentric radii of 6-7 Mpc. The cluster mass measurements from weak-lensing analysis of Subaru observations reaches a typical scaled radius of $r_{200,c}$ (Okabe & Smith 2016). This, combined with the mass information available to us from the X-ray analysis, allow us to experiment with different approaches to stacking the cluster luminosity density profiles – i.e. in physical comoving units, or scaled to a common overdensity radius such as $r_{200,m}$. A visual impression of the

---

[1] http://herschel.as.arizona.edu/acres/acres.html

quality of the data is given in Figure 1, and full details of density profile construction are described in Section 4.

The combined LoCuSS/ACReS dataset also allows us to characterize the structure of clusters. This is important, because the splashback feature in cluster density profiles is associated with infall of material in to the cluster potential, and the structure of clusters seen at different wavelengths is sensitive to their infall history. In addition to stacking all of the 20 clusters, we therefore present results in Section 4 based on sub-dividing the sample in to sub-samples selected based on their structural properties that are motivated by in-fall history. The main results are based on sub-samples selected on the presence of X-ray detected infalling galaxy groups, which indicate active ongoing accretion of galaxies, based on the analysis of Haines et al. (2018). Infalling X-ray groups were identified as extended X-ray sources in our XMM images down to $\approx 2 \times 10^{42}$ erg s^{-1} ($M_{200} \approx 2.5 \times 10^{13}\, M_\odot$) and confirmed to be infalling in to the clusters by identifying group members within the X-ray emitting region of the group with spectroscopic redshifts consistent with that of the host cluster. The X-ray data typically permit us to identify infalling groups within the radial range $0.35 - 1.3\, r_{200}$. In addition we included our own analysis of three clusters not in their sample (A 586, A 2485, and ZwCl 0104.4+0048). We excluded Abell 1689 from the subsample of clusters without infalling groups because of the rich structure of this cluster along the line of sight, which is strongly indicative of ongoing merging activity (Miralda-Escude & Babul 1995; Andersson & Madejski 2004; Peng et al. 2009). In addition, we use proxies for cluster merger history including central entropy, X-ray/BCG offset, X-ray brightness concentration and centroid shift, and luminosity gap, as discussed in Appendix A).

3. DENSITY PROFILE MODELING METHODS

Empirical profiles have proven successful in describing the radial variations of density profiles of dark matter haloes, featuring single or multiple power-law behaviours. Among the latter, Jaffe (Jaffe 1983), Hernquist (Hernquist 1990) and Navarro-Frenk-White (Navarro et al. 1996) share the same functional form, differing only in the inner and outer power-law slopes (see Binney & Tremaine 2008 for a review). Here, we choose to model the inner slope of the density profile with a single power-law prescription (Einasto et al. 1974), corresponding to the virialized part of the halo, together with an additional power-law describing the infall region. These two components are linked by a transitional term which allows for the radial profile to steepen due to the presence of the splashback feature. Following Diemer & Kravtsov (2014) and using the `Colossus` toolkit (Diemer 2018), we adopt the radial density profile $\rho(r)$ accordingly:

$$\rho(r) = \rho_{\text{Ein}}(r) \times f_{\text{trans}}(r) + \rho_{\text{infall}}(r), \qquad (1)$$

$$\rho_{\text{Ein}}(r) = \rho_s \exp\left\{ -\frac{2}{\alpha}\left[\left(\frac{r}{r_s}\right)^\alpha - 1 \right] \right\}, \qquad (2)$$

$$f_{\text{trans}}(r) = \left[1 + \left(\frac{r}{r_t}\right)^\beta \right]^{-\gamma/\beta}, \qquad (3)$$

$$\rho_{\text{infall}}(r) = \frac{\rho_0}{1/\Delta + (r/r_{\text{pivot}})^{s_e}} \qquad (4)$$

with $r_{\text{pivot}} = 1.5$ Mpc. The parameters ρ_s and ρ_0 are inner and infall scale density, respectively. The parameter r_s is the scale radius of the inner profile and r_t is the transition radius between the inner and infall regimes. The exponent α sets the slope of the inner profile, β and γ set the shape and depth of the transition term, and s_e sets the slope of the outer term (Diemer & Kravtsov 2014). The transition function helps in reconstructing the density profile around the splashback feature, which gets smoothed by the radial averaging (Mansfield et al. 2017). The parameter Δ acts as a maximum cutoff density of the outer term to avoid its spurious contribution at small radii. Overall, implementing such truncation has a negligible impact, and we leave this threshold unconstrained. Hence α, β, γ, r_s, r_t, ρ_s, ρ_0 and s_e are the free parameters of the model. We considered also models without transition by setting the parameter $\gamma = 0$. We relate the 2d projected density $\Sigma(R)$ observed from LoCuSS to the 3d density $\rho(r)$ via

$$\Sigma(R) = 2 \int_R^\infty dl\, \frac{\rho(r)r\, dr}{\sqrt{r^2 + R^2}}, \qquad (5)$$

where R is the 2d projected distance from the cluster center. The splashback radius, r_{sp}, is a derived parameter in this model, and represents the minimum of the logarithmic derivative $d\,\text{Log}(\rho)/d\,\text{Log(r)}$ of the density profile.

We perform the estimation of best-fit parameters in the context of Bayesian inference, by computing the posterior distribution

$$P(\vec{\theta}|d, m) = \frac{\mathcal{L}(\vec{\theta})P(\vec{\theta}|m)}{\mathcal{Z}}, \qquad (6)$$

where $\mathcal{L}$ is the likelihood, $P(\vec{\theta}|m)$ is the prior, and $\mathcal{Z}$ is the evidence, for a given model $m(x_i|\theta)$ evaluated at the data point x_i using parameter values specified by $\vec{\theta}$. We adopt a Gaussian likelihood $\mathcal{L}$ for the data $\vec{d} = (x_i, y_i)$, given $\vec{\theta}$:

$$\log \mathcal{L}(\vec{d}|\theta) = -\frac{1}{2} \sum_i^{N_d} \left(\frac{y_i - m(x_i|\theta)}{\sigma_i} \right)^2 + \log \mathcal{N}(N_d, \{\sigma_i\}), \qquad (7)$$

Table 3. Model parameters and their prior properties

Parameter	Prior
ρ_0 [$10^3 \times M_\odot h^2/kpc^3$]	flat:[0.17, 10]
s_e	flat:[0.1, 10]
r_s [Mpc/h]	flat:[0.3, 0.7]
ρ_s [$10^4 \times M_\odot h^2/kpc^3$]	flat:[7, 50]
r_t [Mpc/h]	flat:[1.0, 6.0]
α	flat:[0.1, 0.8]
β	flat:[3.0, 9.0]
γ	flat:[2.0, 7.0]

where σ is the uncertainty on the data, and i cycles over the number of data points. $\mathcal{N}(N_d, \{\sigma_i\})$ acts as normalisation constant to ensure that the integral of the posterior distributions equals to unity.

In this work, we utilise the nested sampling algorithm to compute the Bayesian evidence $\mathcal{Z}$, following the formalism by Skilling (2004) implemented in CPNest (Veitch et al. 2017). Nested sampling advantages include the simultaneous estimates of both evidence and posterior samples, and in being easily parallelizable. By splitting the prior volume over intervals of equal likelihood, the evidence results from simple numerical integration, with the addition of reducing the dimensionality of the problem to 1-d. The algorithm allows to evaluate the posteriors on the model parameters

$$\ln \mathcal{P}(\vec{\theta}|d, m) = \ln \left[\mathcal{L}(\vec{d}|\vec{m}(\vec{\theta})) \Pr(\vec{\theta}|m) \right]. \quad (8)$$

Nested sampling allows to perform model selection based on marginalized likelihood. Therefore we can directly quantify and compare the evidence in the data in favour of models with and without the transition feature. We consider eight free parameters (ρ_0, ρ_s, r_t, r_s, α, β, γ and s_e) from the cluster profile model. While the number of free parameters is large relative to the number of data points, our primary intention here is not to extract robust constraints on the model parameters, but rather to use the model fits to smoothly interpolate the data to extract constraints on the density profile. Despite this, we are able to run to convergence all the fitting procedures using flat priors (see Table 3), without imposing additional a-priori knowledge on the parameter distributions, and to extract data-driven information.

4. ANALYSIS AND RESULTS

4.1. *Constructing the projected density profile*

Stellar mass, and its close relative near-infrared luminosity is tightly correlated with total cluster mass (Mulroy et al. 2014, 2019). In addition, Shirasaki et al. (2021) showed that stellar mass selected galaxy in clusters are good tracers of the gravitational potential of the cluster halo, using the LoCuSS sample. We therefore use spectroscopically confirmed K-band selected cluster galaxies as test particles with which to trace the shape of the cluster density profiles. We then use the mean K-band luminosity of these galaxies and the global cluster K-band mass-to-light ratio to convert our number density profiles in to mass density profiles ready for model fitting using the scheme described in Section 3. As a first step, we select spectroscopically confirmed cluster members galaxies down to K-band magnitude $M_K^* + 1.5$, and use them to compute the stacked clustercentric number density profile, centered on position of the brightest cluster galaxy (BCG), which we adopt as the deepest point of each cluster's potential well. In addition, we assign the mean K-band luminosity of the whole sample to each galaxy. In this way, we blur-out the effects that different evolution histories may have on the individual galaxies, together with removing any clustercentric distance-dependent process, e.g. mass segregation due to gravitational interactions. Therefore, galaxies are treated as test-particles, that trace the gravitational potential well of the clusters.

We have explored a range of radial bin numbers, and converged on 15 equi-numeric bins to optimise the trade-off between sampling and signal-to-noise of the radial profiles, however our results are not sensitive to this choice, with the binning scheme mainly aiding visualization of the data. The projected density $\Sigma(R)$ is then obtained by multiplying the radially-binned k-corrected K-band luminosity by a mass-to-light ratio $M/L = 100$, that is consistent with the multivariate LoCuSS cluster scaling relations (Mulroy et al. 2019), and other studies of intermediate redshift clusters including Muzzin et al. (2007). We have verified that varying the choice of the mass-to-light ratio does not impact or alter the results obtained from the fit presented in Section 3, in particular regarding the detection of the splashback feature. Indeed, the main motivation for converting light to mass is simply to facilitate the fitting of mass density profiles in Section 3.

Following Haines et al. (2013), each galaxy is weighted by the inverse probability of having being observed spectroscopically. Furthermore, we include an additional weight accounting for the fractional coverage from the near-infrared UKIRT footprint of the circular annuli used to produce the radially-averaged density profiles a function of clustercentric distance. This allows us to quantify the spatial and spectroscopic completeness of our data as a function of increasing clustercentric distance. In particular, we choose to restrict our density profiles to a radius cut corresponding to a weight threshold w < 2, which encompasses the area within which more than 50% of the galaxies assumed in the analysis are detected. Figure 1 allows us to appreciate more clearly the radial completeness of our sample. In particular, we can see

Full cluster sample   **Clusters w/o groups**   **Clusters with groups**
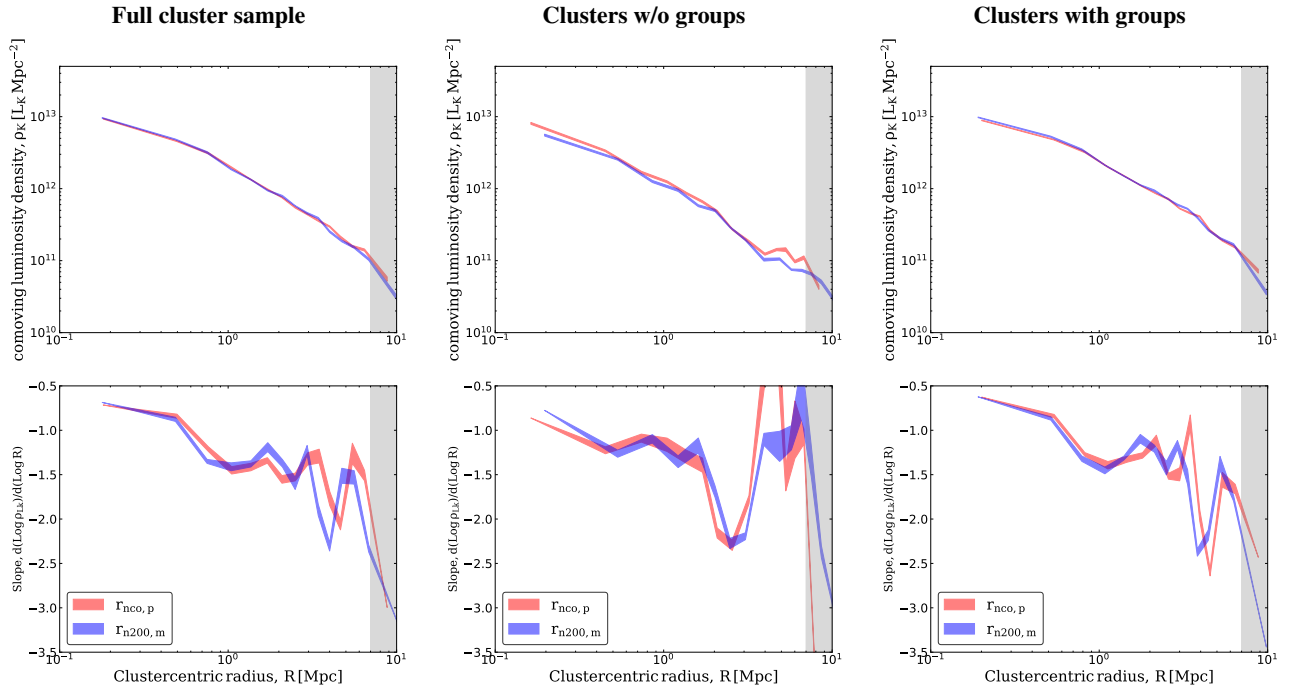
Figure 2. Top panels: luminosity density profile of the stacked clusters galaxies, computed assigning to each galaxy the mean K-band luminosity of the total sample, using non-scaled and scaled radii according to $r_{200,m}$ shown in red and blue respectively. From left to right, we show the profile of the total cluster sample, and the clusters without and with infalling groups. Bottom panel: logarithmic slope of the luminosity density profile. The colored bands encompasses the errors which are computed from the standard deviation of the mean density within each bin.

a steep decrease occurring in the profiles beyond $2.5\,r_{200,m}$, which is marked by the grey area. This corresponds to the clustercentric distance at which our sample average completeness weight exceeds the $w < 2$ threshold discussed above. We note a similar occurring when considering a sample of coeval field galaxies drawn from the LoCuSS dataset, selected in the background and foreground of the clusters (Haines et al. 2015), which confirms that the completeness threshold is a property of the data, and not related to cluster properties.

In Figure 1, we show different luminosity profiles computed by arranging the stacked galaxy clustercentric radii according to a range of overdensity thresholds, i.e. $r_{200,m}$, $r_{200/500,c}$, r_{vir} and $r_{500,x}$. In particular, we consider density contrast with respect to the critical (c) and matter density (m) of the Universe, and with virial radius obtained from weak-lensing and X-ray (x) data respectively. The mean value of these radii for the entire cluster sample is shown by the dashed vertical lines. We note an increasingly self-similar behaviour of the luminosity density profiles when scaled using critical and matter density of the Universe, with respect to the profile computed without using any scaling threshold, marked as $r_{co,p}$ in the figure. Numerical simulations have shown that the outermost density profiles in clusters at $r > r_{200,m}$ are self-similar when the radii are scaled by $r_{200,m}$ (or, more generally, by any radius that is defined with respect to the mean density). This self-similarity indicates that radii defined with respect to the mean density are preferred to describe the structure

and evolution of the outer profiles. By contrast, the inner density profiles at smaller radii are most self-similar when radii are scaled by $r_{200,c}$ (Diemer & Kravtsov 2014). In the following analysis, and in particular regarding fitting, we consider profiles scaled according to $r_{200,m}$ from Okabe & Smith's weak-lensing measurements.

4.2. *Empirical detection of splashback feature*

Figure 2 (top-left panel) shows the luminosity density profile of the total cluster sample. A dip in the density profile can be noted around 4 Mpc. This feature appears more clearly (bottom-left panel) when plotting the logarithmic slope of the profile $\epsilon = d\,\mathrm{Log}(\rho)/d\,\mathrm{Log}(R)$, and extends between 3 and 5 Mpc, peaking at 4 Mpc where it reaches $\epsilon = -2.30 \pm 0.06$. This has a significance of 5.9σ with respect to the mean slope value of $\epsilon = -1.55 \pm 0.11$ at neighboring radii. The location of this feature in the density profile, and the run of slope with radius that we obtain are typical of what has been predicted from numerical simulations (Diemer & Kravtsov 2014), even when considering the 2-d surface density. In Figure 2, we show also the density profiles of the cluster sample, split according to the presence of infalling X-ray groups in their surroundings. Interestingly, we notice that the sharp splashback feature, which clearly appears in both sub-samples occurs at smaller radii when considering clusters without infalling X-ray groups. In particular the splashback feature peaks around 2.5 Mpc with a slope of $\epsilon = -2.23 \pm 0.07$ at

Parameter	Sample		
and Marginalized posterior	Total	without infalling groups	with infalling groups
ρ_0 [$10^3 \times \mathrm{M_\odot h^2/kpc^3}$]	$4.43^{+1.41}_{-1.49}$	$2.72^{+0.83}_{-0.88}$	$4.11^{+2.01}_{-2.05}$
s_e	$1.75^{+0.15}_{-0.16}$	$1.61^{+0.15}_{-0.16}$	$1.46^{+0.19}_{-0.20}$
r_s [Mpc/h]	$0.48^{+0.01}_{-0.01}$	$0.48^{+0.05}_{-0.05}$	$0.58^{+0.02}_{-0.02}$
ρ_s [$10^5 \times \mathrm{M_\odot h^2/kpc^3}$]	$246.5^{+22.1}_{-24.4}$	$150.7^{+30.3}_{-33.6}$	$186.3^{+12.3}_{-12.3}$
r_t [Mpc/h]	$4.18^{+1.00}_{-0.87}$	$1.81^{+0.14}_{-0.15}$	$2.78^{+0.11}_{-0.12}$
α	$0.27^{+0.02}_{-0.02}$	$0.19^{+0.05}_{-0.05}$	$0.20^{+0.02}_{-0.02}$
β	> 6	> 6	> 6
γ	> 4	> 4	> 4
$r_{200,\mathrm{m}}$ [Mpc/h]	2.19 ± 0.01	1.74 ± 0.01	2.35 ± 0.01
$M_{200,\mathrm{m}}$ [$10^{14} \times \mathrm{M_\odot/h}$]	14.11 ± 0.12	6.84 ± 0.13	17.64 ± 0.18
r_{sp} [Mpc/h]	3.83 ± 0.75	2.01 ± 0.12	3.04 ± 0.15
max(Log slope 3d)	$-3.4^{+0.7}_{-0.6}$	$-4.2^{+0.7}_{-0.2}$	$-4.4^{+0.9}_{-0.2}$

Table 4. Parameters of the best-fit model resulting from the fit of the full cluster sample, and classified according to the presence of infalling groups. The errors quoted in the individual parameters are estimated from their posterior distribution and encompass the 15 and 85% percentile. The table includes also marginalized posteriors, i.e $r_{200,\mathrm{m}}$, $M_{200,\mathrm{m}}$, and 3-d splashback radius r_{sp} and their $\pm 3\sigma$ intervals. In addition we quote the minimum values of the 3-d logarithmic slope of the density profile.

6.5σ for clusters with no infalling groups and peaks at 3.8 Mpc a slope of $\epsilon = -2.37 \pm 0.06$ at 6.1σ for the systems with infalling groups. Furthermore, we notice that the splashback feature appears consistently at the same location, whether considering scaled or non-scaled radii, for clusters without in-falling groups. This is consistent with clusters that not actively accreting groups having more self-similar structure than clusters that are actively accreting.

We note a similar picture when classifying the clusters using the different structural parameters (see Appendix A: Figures 6 & 7). Specifically, cluster sub-samples that are discussed in the literature variously as relaxed, undisturbed, or dynamically quiet (e.g. based on low central entropies, small X-ray centroid shift, large luminosity gap) have a more prominent splashback feature, appearing at smaller clustercentric radii than their so-called unrelaxed, disturbed, or dynamically more active cousins. The consistency of this picture is very striking because the structural parameters used to define the different sub-samples span a wide range of scales, from central entropy on scales of 20kpc through to the presence of X-ray emitting infalling groups at 1-3Mpc.

4.3. Measurement of splashback radius in 3-dimensions

We performed the model fit to the entire cluster sample and to sub-samples classified by the presence and absence of infalling groups, as shown in Figure 3. The best-fit parameters, together with salient properties of the best-fit model are summarised in Table 4. From the full cluster sample, we recover a ratio between the 3-d splashback radius and $r_{200,\mathrm{m}}$ of $r_{\mathrm{sp}}/r_{200,\mathrm{m}} = 1.74 \pm 0.34$ and cluster masses consistent with Okabe & Smith's weak-lensing analysis.

As expected based on the results in Section 4.2, the 3-dimensional splashback radius of clusters without infalling groups, $r_{\mathrm{sp}}/r_{200,\mathrm{m}} = 1.158 \pm 0.071$, is smaller than for clusters with infalling groups $r_{\mathrm{sp}}/r_{200,\mathrm{m}} = 1.291 \pm 0.062$. This difference between the sub-samples is significant at 4.2σ, and persists if we remove the spectroscopically confirmed infalling group members from the cluster member sample. Masses $M_{200,\mathrm{m}}$ for both haloes with and without infalling groups are in agreement with the ones recovered from the weak-lensing analysis by Okabe & Smith (2016). We stress that our dataset is sensitive to the detection of massive infalling groups and retains completeness down to galaxy stellar masses of $M_\star = 2 \times 10^{10}\,\mathrm{M_\odot}$ (Haines et al. 2018). Therefore, sampling the full mass range of halo accretion on clusters in beyond the reach of this dataset, hence a direct comparison with simulations remains challenging because predictions that match our observational sample are not yet available.

Among the parameters considered in the fit, we note looser constraints obtained for β and γ. These parameters are known to be related to the accretion rate of haloes, as shown by numerical simulations (Diemer & Kravtsov 2014), and can jointly span the prior space even in case of haloes with similar properties. This degeneracy is known and has been mitigated by imposing stringent log-normal priors in the literature (Shin et al. 2019; Murata et al. 2020). We have chosen to not adopt this restriction in our study, after verifying the low impact of the flat priors choice on the fit. In particular, we obtain density profile slopes which are below values of -3, which is the lower limit of NFW profiles, when considering the full extent of the posteriors obtained for β and γ. This result provides further evidence of the splashback feature. The
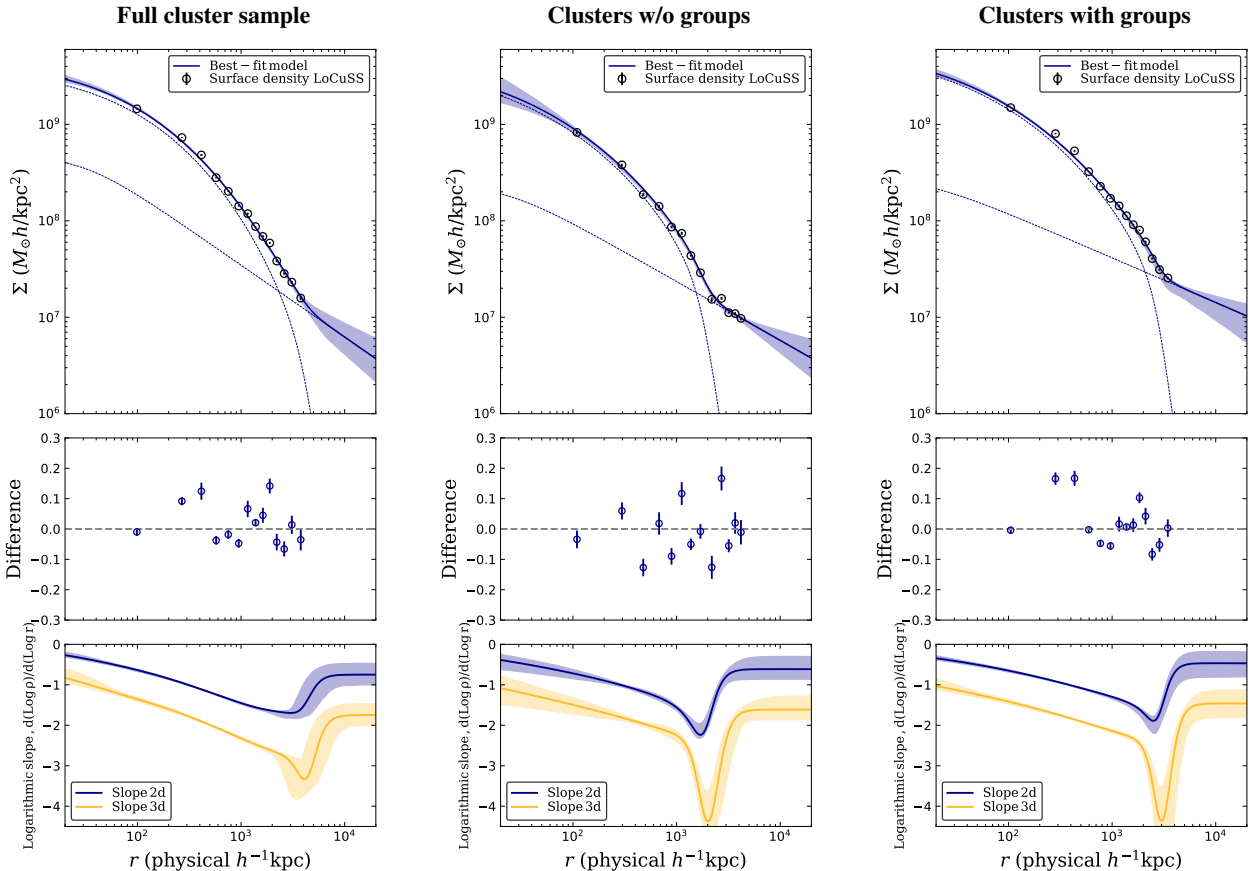
Figure 3. Data points and best-fit models for the entire cluster sample (left panel), cluster with no infalling groups (middle panel) and cluster with infalling groups (right panel). For each column, top panel: black circles show the observed surface density profile. Theoretical profile from Section 3 is fitted and plotted as comparison, in dark blue. The profile is split in to its inner and outer components, plotted as dashed lines. Middle panel: difference between the theoretical fitted profiles and data points. Bottom panel: 2D and 3D slopes of the best-fit theoretical model. The shaded area shows the 15 and 85 percentile extracted from the likehood distribution.

corner plot presenting the distribution of the posteriors of each parameters are shown in Figure 8 in Appendix A.

The Bayesian framework that we used through the CPNest implementation allowed us to directly compare the models, with and without splashback features, and determine which one is preferred according to the data-driven information. In particular, we can compute directly the Bayes factor $\mathcal{B}$ from the evidence of the two models extracted from the fitting procedure in CPNest, under the assumption of equal and uniform priors. We report a Bayes factor in excess of $\mathcal{B} > 100$ in favour of the model with a splashback feature when considering the profiles of clusters without infalling groups. This is the dataset showing the strongest signature of the splashback feature among the ones considered here. The fit to the model without feature outputs a skewed posterior of the ρ_0 parameter towards the lower limit of the prior. This limit corresponds to the critical matter density of the Universe at the redshift considered, and bounds the density domain of the infalling part of the model (Diemer & Kravtsov 2014). This is further evidence of the necessity of a model including a density tran-

sition to describe the data profiles. Furthermore, by fitting the same models with the same priors to the data excised of the transition region, we obtain a Bayes factor $\mathcal{B} < 0.6$, favouring the model not allowing for the splashback transition.

5. SUMMARY AND DISCUSSION

5.1. *Summary of results*

We report the detection of the splashback feature in a sample of massive clusters at intermediate redshifts. The feature is detected using the luminosity density profile of the stacked sample of clusters, computed using the K-band magnitude of spectroscopically confirmed cluster members. Hereafter we list the main results of our analysis:

- We empirically detect the splashback feature at a significance greater than 5σ. This holds true for the case of the total cluster sample, and for the clusters classified according to the presence/absence of infalling groups.

- We have fitted the observed projected density profiles using the models suggested by Diemer & Kravtsov
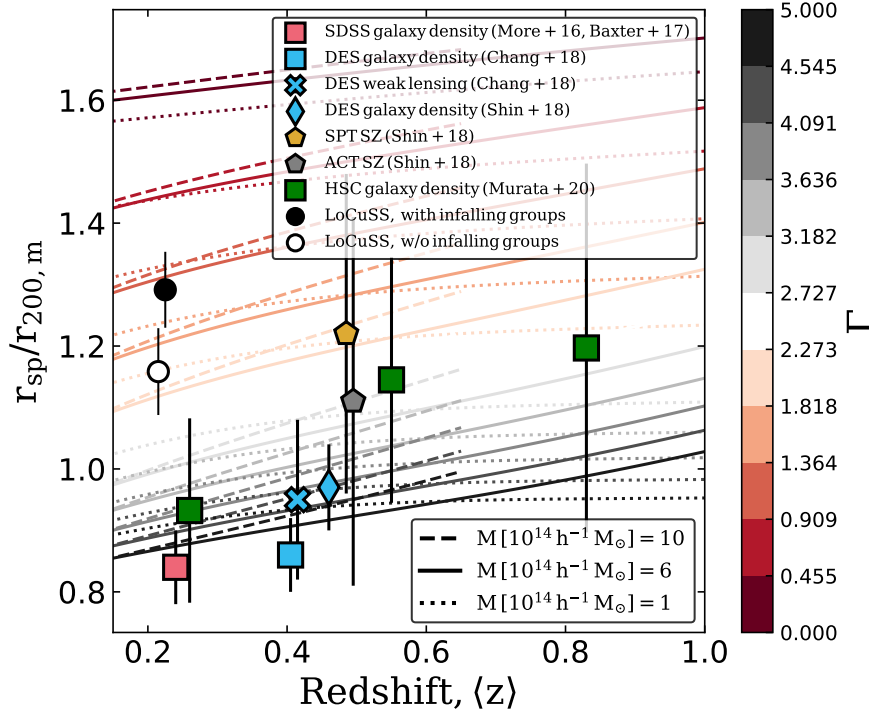
Figure 4. Summary of the literature measurements of the 3d splashback feature r_{sp}, normalized by $r_{200,m}$, plotted with respect to the mean redshift of the data considered. The shape of the symbol codes the method used for the cluster and galaxy selection, as listed in the corresponding literature reference, and the colour codes the dataset used. LoCuSS datapoint are artificially offset along the x-axis to improve visibility. The background lines mark the redshift evolution of the splashback radius of three reference haloes with masses $M_{200,m}[10^{14}\,h^{-1}\,M_\odot] \in \{10, 6, 1\}$ as a function of a range of accretion rates, defined as logarithmic mass increment over one dynamical timescale from the empirical relation for cluster-like halo model by Diemer et al. (2017).

(2014), in the context of Bayesian inference in combination with the nested sampling method. This allowed us to recover salient properties of the cluster haloes, including position of the splashback radius relative to $r_{200,m}$. The Bayes factor rates the model allowing for the splashback transition as better describing the data.

- The splashback feature position shows a strong dependency according to the presence of infalling groups. Clusters with no detected massive infalling groups present the splashback feature at $r_{sp}/r_{200,m} = 1.158 \pm 0.071$, with respect to cluster accreting groups showing $r_{sp}/r_{200,m} = 1.291 \pm 0.062$, different at 4.2σ significance. This suggests a correlation between the properties of the cluster potential and its accretion rate. We thus report the first measurement of the impact of ongoing accretion and mergers on the measurement of the splashback radius.

- Clusters that are classified as old and dynamically inactive present stronger signatures of the splashback feature, with respect to younger, more active clusters. This is not surprising as the latter are bound to show lesser

degrees of self-similarity in their density profiles, due to ongoing disturbance caused by accretion and mergers. We showed that dynamical properties, despite being defined within the cluster central regions, describe cluster properties which reverberates out to the cluster outskirts.

5.2. *Comparison with simulations*

In Figure 4, we can see the trend of $r_{sp}/r_{200,m}$ with respect to redshift. For comparison, the background lines mark the theoretical trend of the ratio $r_{sp}/r_{200,m}$ as a function of halo accretion rate, which is defined as the logarithmic variation of the cluster mass within one dynamical timescale ($\approx 1\,\text{Gyr}$) from Diemer et al. (2017). Simulations have shown that actively-accreting clusters present a contraction of the splashback radius, correlating with accretion rate. In this work, we observe the opposite behaviour. Sorce et al. (2020) analysed a set of cluster halos from the MultiDark simulation to find that cluster halos with massive neighbours (with masses above about 10% of the cluster halos) within $2 - 4 \times r_{vir}$ had quieter cluster assembly histories recently than on average, and were more active beyond $z \approx 1$. These halos indeed did

not accrete their close-by halos and thus did not empty their neighbourhood. On the contrary, a low number of neighbors in the same distance range is linked to the opposite scenario, namely recently active and quieter in the past. This helps to reconcile our findings with the results from simulations by Diemer & Kravtsov (2014). The clusters showing massive infalling groups are about to enter a phase of substantial accretion, which will result in a contraction of the splashback radius. We nevertheless stress the challenges of capturing the full extent of halo accretion in observed clusters, which is composed of a continuous stream of haloes of widely different masses. As shown in Diemer & Kravtsov (2014); Diemer et al. (2017) and in Figure 4, the ratio $r_{sp}/r_{200,m}$ shows the strongest dependence with mass accretion rate. Additionally, at fixed r_{sp}, the ratio $r_{sp}/r_{200,m}$ depends non-trivially on halo mass, accretion rate and redshift (Diemer et al. 2017). We note that our results do not show strong dependence on the redshift and halo mass as a result of the narrow interval of both for the cluster sample considered here. Hence, we can further ascribe the observed trend of the ratio $r_{sp}/r_{200,m}$ to the accretion rate of clusters. We note that the cluster sample with and without groups are characterised by discrepant mean masses, with the former larger by a factor of ≈ 2.6. A similar mass separation is found when using the different proxies for cluster dynamical state. However, this is not a major source of systematic uncertainty in our results because the differences in the assembly rate of clusters over the mass and redshift range under consideration are minimal (Pizzardo et al. 2020). Following the Press and Schechter formalism (Lacey & Cole 1993), the typical mass of infalling haloes is approximately 10% of the mass of main accreting halo, implying that the typical infalling group mass is correlated with the cluster mass. Therefore, we argue that the detection of infalling groups via X-ray emission in less massive clusters will be impeded by survey limits more than in more massive clusters. This is coupled with the luminosity boost of bright X-ray cluster cores, which impacts favourably the detection of less massive clusters. Crucially, our study confirms that massive clusters are undergoing continuous accretion of group-like haloes, which does not affect the presence of the splashback feature as drastically as for clusters classified via different dynamical proxies (e.g. central entropy). This could be related to the different timescales considered by the different proxies, and with respect to simulations (Diemer & Kravtsov 2014; Diemer et al. 2017), and requires further investigation. Overall, the whole cluster sample provides the less stringent constraints on the recovered splashback feature resulting in a ratio between the 3-d splashback radius and $r_{200,m}$ of $r_{sp}/r_{200,m} = 1.74 \pm 0.34$. This supports the scenario in which the dynamical state of individual clusters dilutes the stacked signal of the splashback feature.

5.3. *Comparison with previous observations*

Figure 4 summarises recently attempted measurements of the splashback feature in cluster samples by means of different observational approaches which include member optical photometric selection (More et al. 2015; Baxter et al. 2017; Chang et al. 2018; Shin et al. 2019; Murata et al. 2020, see also Trevisan et al. 2017), weak-lensing (Chang et al. 2018), and SZ (Shin et al. 2019). Our measurements based on the spectroscopically confirmed cluster galaxies lends further weight to the critical importance of using cluster selection methods based on galaxy membership (cfr. Shin et al. 2019), in terms of both significance and reduction of contamination from interlopers (More et al. 2015; Busch & White 2017). In particular, note that in Figure 4 we plot 3σ errorbars for data points from our work, and 1σ intervals for measurements from the literature. We stress the 4.2σ discrepancy in the ratio $r_{sp}/r_{200,m}$ between clusters with and without accreting groups. Richness-based methods (More et al. 2015; Busch & White 2017; Chang et al. 2018) appear to underestimate the radius at with the splashback transition occurs, partly due to galaxy interloper contamination. Our cluster member selection based on spectroscopic redshifts allows for an efficient removal of field contaminants, and our results are consistent with the model predictions from Murata et al. (2020).

5.4. *Future outlook*

Future large-scale surveys, namely *eRosita*, the Vera Rubin Observatory (Ivezić et al. 2019), and 4MOST (de Jong et al. 2019), will provide crucial multiwavelength data to sample with greater statistical significance the accretion rates of estimated $\approx 10^5$ clusters, extending the detection of spectroscopically confirmed cluster members and infalling halos at increasing clustercentric distances. Interestingly, Deason et al. (2021) suggest that the next generation instruments will allow the detection of the splashback feature for the diffuse stellar intracluster light. Understanding the individual impact of halo mass, accretion rate and redshift evolution is currently still an open question, answering which will help towards a more complete description of the fine-grained growth of cosmological structures. Our intent is to promote further discussion between simulations and observations, in particular regarding observational proxies of halo accretion rates.

---

[2] http://www.benediktdiemer.com/code/colossus/

REFERENCES

Adhikari, S., Dalal, N., & Chamberlain, R. T. 2014, JCAP, 2014, 019

Adhikari, S., Shin, T.-h., Jain, B., et al. 2020, arXiv e-prints, arXiv:2008.11663

Andersson, K. E., & Madejski, G. M. 2004, ApJ, 607, 190

Babul, A., Balogh, M. L., Lewis, G. F., & Poole, G. B. 2002, MNRAS, 330, 329

Baxter, E., Chang, C., Jain, B., et al. 2017, ApJ, 841, 18

Bertschinger, E. 1985, ApJS, 58, 39

Bianconi, M., Smith, G. P., Haines, C. P., et al. 2018, MNRAS, 473, L79

Bildfell, C., Hoekstra, H., Babul, A., & Mahdavi, A. 2008, MNRAS, 389, 1637

Binney, J., & Tremaine, S. 2008, Galactic Dynamics: Second Edition

Böhringer, H., Schuecker, P., Guzzo, L., et al. 2004, A&A, 425, 367

Bryan, G. L., & Norman, M. L. 1998, ApJ, 495, 80

Bullock, J. S., Kolatt, T. S., Sigad, Y., et al. 2001, MNRAS, 321, 559

Busch, P., & White, S. D. M. 2017, MNRAS, 470, 4767

Cassano, R., Ettori, S., Giacintucci, S., et al. 2010, ApJL, 721, L82

Chang, C., Baxter, E., Jain, B., et al. 2018, ApJ, 864, 83

Cole, S., & Lacey, C. 1996, MNRAS, 281, 716

de Jong, R. S., Agertz, O., Berbel, A. A., et al. 2019, The Messenger, 175, 3

De Lucia, G., Weinmann, S., Poggianti, B. M., Aragón-Salamanca, A., & Zaritsky, D. 2012, MNRAS, 423, 1277

Deason, A. J., Oman, K. A., Fattahi, A., et al. 2021, MNRAS, 500, 4181

Diemand, J., Kuhlen, M., & Madau, P. 2007, ApJ, 667, 859

Diemer, B. 2018, ApJS, 239, 35

Diemer, B., & Kravtsov, A. V. 2014, ApJ, 789, 1

Diemer, B., Mansfield, P., Kravtsov, A. V., & More, S. 2017, ApJ, 843, 140

Diemer, B., More, S., & Kravtsov, A. V. 2013, ApJ, 766, 25

Ebeling, H., Edge, A. C., Bohringer, H., et al. 1998, MNRAS, 301, 881

Eckert, D., Molendi, S., Owers, M., et al. 2014, A&A, 570, A119

Einasto, J., Kaasik, A., & Saar, E. 1974, Nature, 250, 309

Farahi, A., Ho, M., & Trac, H. 2020, MNRAS, 493, 1361

Farahi, A., Mulroy, S. L., Evrard, A. E., et al. 2019, Nature Communications, 10, 2504

Fillmore, J. A., & Goldreich, P. 1984, ApJ, 281, 1

Gozaliasl, G., Finoguenov, A., Khosroshahi, H. G., et al. 2014, A&A, 566, A140

Gunn, J. E., & Gott, III, J. R. 1972, ApJ, 176, 1

Haines, C. P., Pereira, M. J., & et al., S. 2013, ApJ, 775, 126

—. 2015, ApJ, 806, 101

Haines, C. P., Pereira, M. J., Sanderson, A. J. R., et al. 2012, ApJ, 754, 97

Haines, C. P., Finoguenov, A., Smith, G. P., et al. 2018, MNRAS, 477, 4931

Hernquist, L. 1990, ApJ, 356, 359

Hinton, S. R. 2016, The Journal of Open Source Software, 1, 00045

Ivezić, Ž., Kahn, S. M., Tyson, J. A., et al. 2019, ApJ, 873, 111

Jaffe, W. 1983, MNRAS, 202, 995

Lacey, C., & Cole, S. 1993, MNRAS, 262, 627

Mahdavi, A., Hoekstra, H., Babul, A., et al. 2013, The Astrophysical Journal, 767, 116

Mansfield, P., Kravtsov, A. V., & Diemer, B. 2017, ApJ, 841, 34

Martino, R., Mazzotta, P., Bourdin, H., et al. 2014, MNRAS, 443, 2342

Maughan, B. J., Jones, L. R., Pierre, M., et al. 2008, MNRAS, 387, 998

McGee, S. L., Balogh, M. L., Bower, R. G., Font, A. S., & McCarthy, I. G. 2009, MNRAS, 400, 937

Miralda-Escude, J., & Babul, A. 1995, ApJ, 449, 18

More, S., Diemer, B., & Kravtsov, A. V. 2015, ApJ, 810, 36

Mostoghiu, R., Knebe, A., Cui, W., et al. 2019, MNRAS, 483, 3390

Mulroy, S. L., Smith, G. P., Haines, C. P., et al. 2014, MNRAS, 443, 3309

Mulroy, S. L., Farahi, A., Evrard, A. E., et al. 2019, MNRAS, 484, 60

Murata, R., Sunayama, T., Oguri, M., et al. 2020, arXiv e-prints, arXiv:2001.01160

Muzzin, A., Yee, H. K. C., Hall, P. B., & Lin, H. 2007, ApJ, 663, 150

Navarro, J. F., Frenk, C. S., & White, S. D. M. 1996, ApJ, 462, 563

Okabe, N., & Smith, G. P. 2016, MNRAS, 461, 3794

Okabe, N., Smith, G. P., Umetsu, K., Takada, M., & Futamase, T. 2013, ApJL, 769, L35

Peng, E.-H., Andersson, K., Bautz, M. W., & Garmire, G. P. 2009, The Astrophysical Journal, 701, 1283

Pizzardo, M., Di Gioia, S., Diaferio, A., et al. 2020, arXiv e-prints, arXiv:2005.11562

Planck Collaboration, Ade, P. A. R., Aghanim, N., et al. 2016, A&A, 594, A13

Poggianti, B. M., Fasano, G., Omizzolo, A., et al. 2016, AJ, 151, 78

Ponman, T. J., Allan, D. J., Jones, L. R., et al. 1994, Nature, 369, 462

Poole, G. B., Fardal, M. A., Babul, A., et al. 2006, MNRAS, 373, 881

Prada, F., Klypin, A. A., Simonneau, E., et al. 2006, ApJ, 645, 1001

Pratt, G. W., Arnaud, M., Biviano, A., et al. 2019, SSRv, 215, 25

Reiprich, T. H., Basu, K., Ettori, S., et al. 2013, SSRv, 177, 195

Rykoff, E. S., Rozo, E., Busha, M. T., et al. 2014, ApJ, 785, 104

Sanderson, A. J. R., Edge, A. C., & Smith, G. P. 2009, MNRAS, 398, 1698

Schaller, M., Frenk, C. S., Bower, R. G., et al. 2015, MNRAS, 452, 343

Shi, X. 2016, MNRAS, 459, 3711

Shin, T., Adhikari, S., Baxter, E. J., et al. 2019, MNRAS, 487, 2900

Shirasaki, M., Egami, E., Miyazaki, S., & Okabe, N. 2021, arXiv e-prints, arXiv:2101.01342

Skilling, J. 2004, in American Institute of Physics Conference Series, Vol. 735, American Institute of Physics Conference Series, ed. R. Fischer, R. Preuss, & U. V. Toussaint, 395–405

Smith, G. P., Haines, C. P., Pereira, M. J., et al. 2010, A&A, 518, L18

Smith, G. P., Mazzotta, P., Okabe, N., et al. 2016, MNRAS, 456, L74

Sorce, J. G., Gottlöber, S., & Yepes, G. 2020, MNRAS, arXiv:2007.03695

Springel, V., Pakmor, R., Pillepich, A., et al. 2018, MNRAS, 475, 676

Sunyaev, R. A., & Zeldovich, Y. B. 1972, Comments on Astrophysics and Space Physics, 4, 173

Tinker, J., Kravtsov, A. V., Klypin, A., et al. 2008, ApJ, 688, 709

Tomooka, P., Rozo, E., Wagoner, E. L., et al. 2020, MNRAS, arXiv:2003.11555

Trevisan, M., Mamon, G. A., & Stalder, D. H. 2017, MNRAS, 471, L47

Umetsu, K., & Diemer, B. 2017, ApJ, 836, 231

Veitch, J., Del Pozzo, W., & Cody. 2017, Johnveitch/Cpnest: Beta Release, doi:10.5281/zenodo.322819

Voit, G. M. 2005, Reviews of Modern Physics, 77, 207

Walker, S., Simionescu, A., Nagai, D., et al. 2019, SSRv, 215, 7

Zu, Y., Mandelbaum, R., Simet, M., Rozo, E., & Rykoff, E. S. 2017, MNRAS, 470, 551

Zürcher, D., & More, S. 2019, ApJ, 874, 184

APPENDIX

A. CLUSTER STRUCTURE

We have explored how classifying clusters using different proxies of their dynamical state tracing the properties of the central regions, reverberates at greater radii on the splashback feature. These proxies include central entropy, X-ray surface brightness morphology, i.e. concentration and centroid-shift, K-band luminosity gap between the two most luminous galaxies, the offset between X-ray peak emission and BCG location. We follow Mulroy et al. (2019) in using the entropy measurements of Sanderson et al. (2009) to divide the clusters in to those with stronger cooling based on $K_0(< 20\,\mathrm{kpc}) < 80\,\mathrm{keV\,cm^{-2}}$ and those with less strong cooling, i.e. larger values of K_0. The X-ray concentration parameter is defined as the ratio of surface brightness at two characteristic radii, the first encompassing the typical size of cool cores and the second the majority of X-ray emission $c_\mathrm{sb} = \frac{S_X\,(<40\,\mathrm{kpc})}{S_X\,(<400\,\mathrm{kpc})}$, to maximise the dichotomy between the surface brightness distribution of cool-core and non cool-core clusters (Cassano et al. 2010). Here, we utilize the concentration measures from Mulroy et al. (2019), who extracted it from the X-ray surface brightness maps from *Chandra/ACIS-I* and *XMM–Newton/EPIC* observations. Similarly, the measure of the position of the X-ray emission centroid in circular apertures of increasing radii has been used to label cluster merger activity. In particular, high standard deviation ($\langle w\,[0.01\,r_{500,\mathrm{x}}]\rangle > 1$) of the centroid peak has been associated with dynamically disturbed clusters (Poole et al. 2006; Maughan et al. 2008; Mahdavi et al. 2013). Here we use the measures from Martino et al. (2014), cautioning about projection effects which could hide ongoing line-of-sight mergers.

The properties of the brightest cluster galaxy (BCG) can help identifying the formation history of the halo in which it is hosted. In particular, the older the halo, the higher the magnitude gap between the BCG and the second most luminous galaxies (Ponman et al. 1994; Gozaliasl et al. 2014; Farahi et al. 2020). This is due to the action of dynamical friction which facilitates the fall of massive galaxies towards the deep end of the cluster potential where the BCG resides. Subsequent mergers result in a dominant central object surrounded by smaller galaxies. We select a threshold value of the K-band magnitude-gap $\Delta m_{\mathrm{k},12} = 0.5$ (Smith et al. 2010), dividing the bimodal distribution of the full sample.

Bridging between the information provided by the ICM emission and the BCG luminosity, the projected offset between the peak of the X-ray emission and the bulk of the stellar light from the BCG can reveal ongoing cluster dynamical activity (Bildfell et al. 2008). In particular, in case of old and dynamically-quiet clusters, the X-ray emission and the BCG should coincide indicating the deep core of the cluster potential well. Following Sanderson et al. (2009), we select a threshold value of $0.03\,r_{500,\mathrm{wl}}$. Figure 5 summarises the distributions of the dynamical proxies considered of the parent high-L_X LoCuSS sample, and of the cluster sub-sample used in this work.

B. PROFILES

Figure 6 and 7 show the density profiles of clusters classified according to dynamical proxies as presented in Section A. Figure 8 shows corner plots of the parameters posterior distribution from the fit of the density profiles of clusters with and without infalling groups.
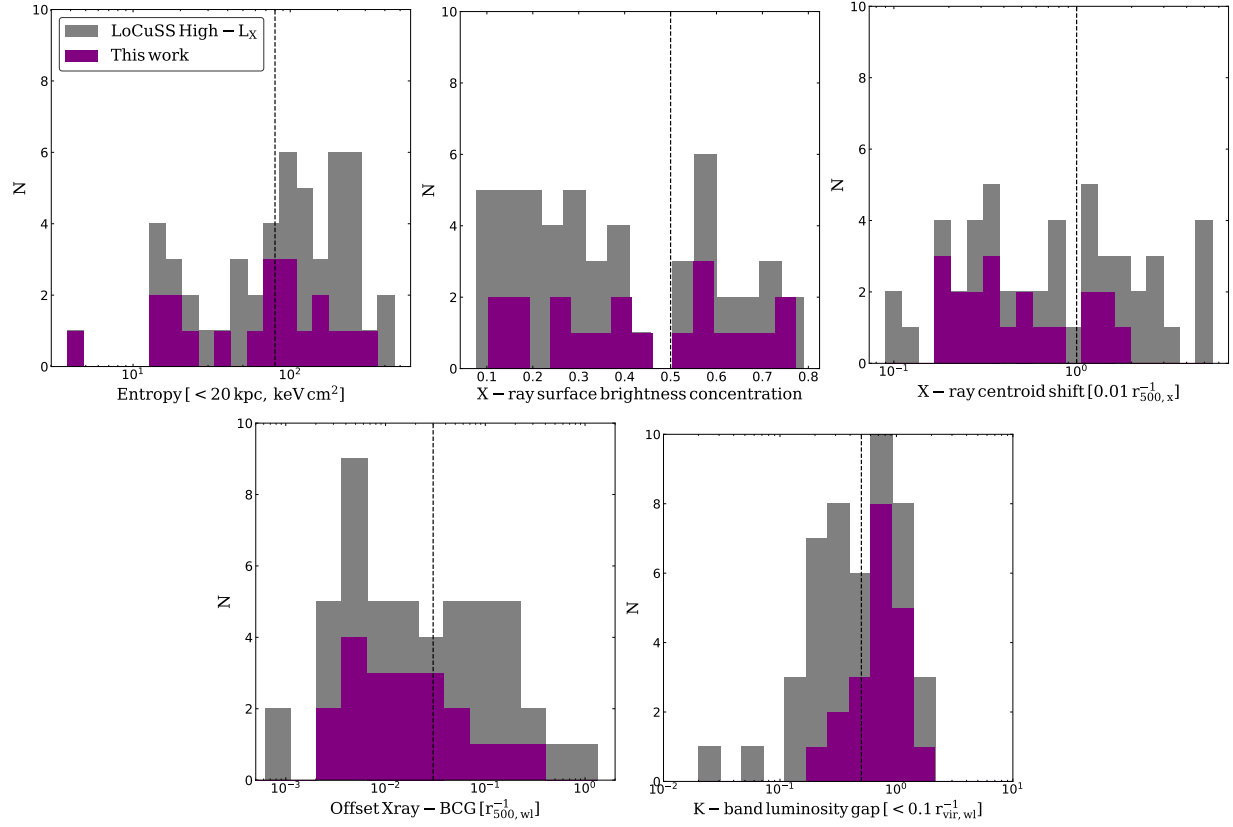
Figure 5. Distributions of the salient cluster properties used to classify their dynamical state and formation timescales, as presented in Section A. From the top-left to the bottom-right, the panels show the central entropy S (< 20 kpc), the X-ray surface brightness concentration and centroid shift, the offset between X-ray emission peak and BCG position, and the k-band magnitude gap, respectively. In each panel, the hatched gray and purple histograms show the distribution of the high-L_X LoCuSS sample and subsample presented in Section 2. The vertical dashed line shows the threshold used to split the sample and produce the plots in Figure 6 and 7
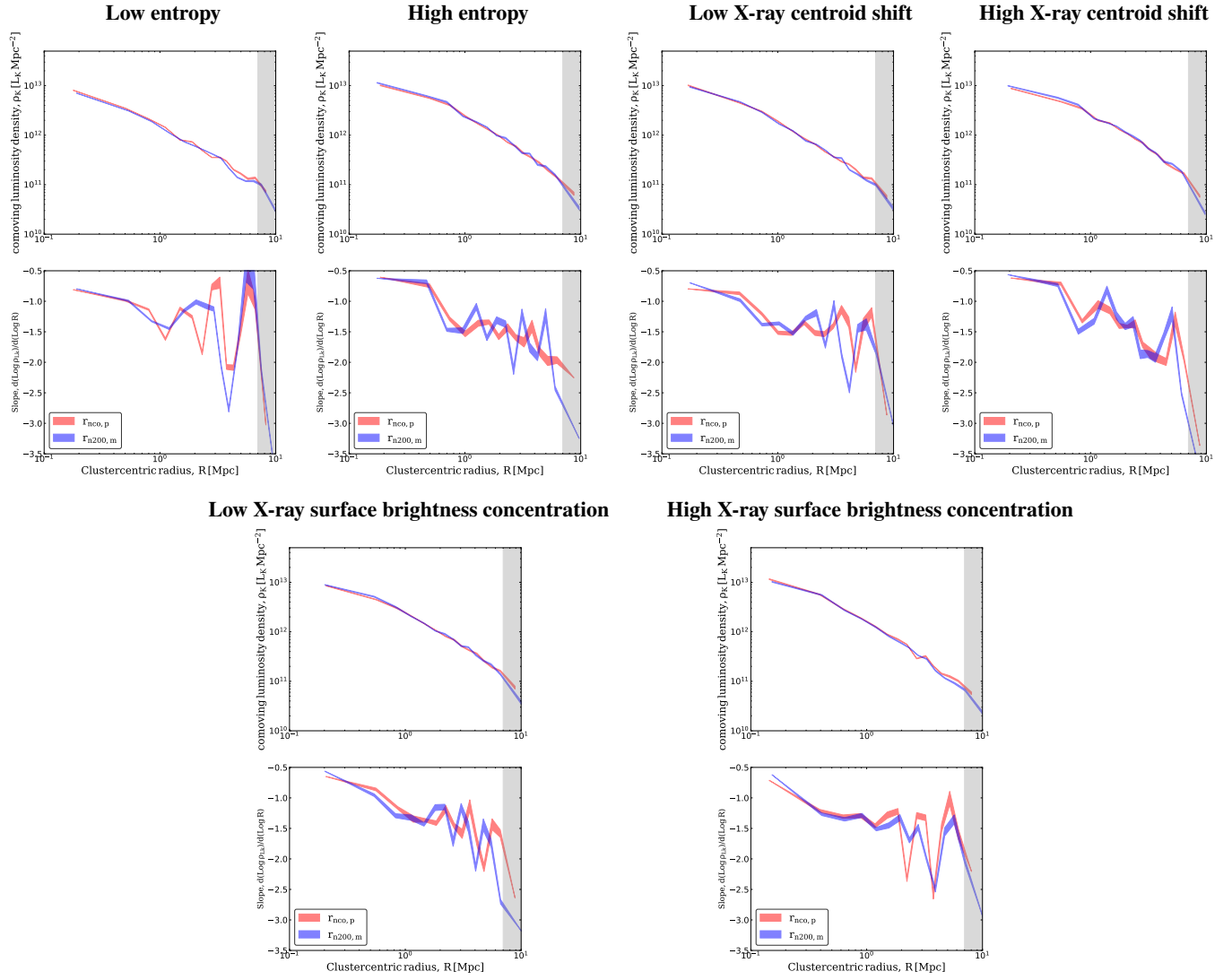
Figure 6. In each subpanel, density profiles (top) and slopes (bottom) resulting from the cluster classification according to the different dynamical proxies presented in Section A. Continues in Figure 7.
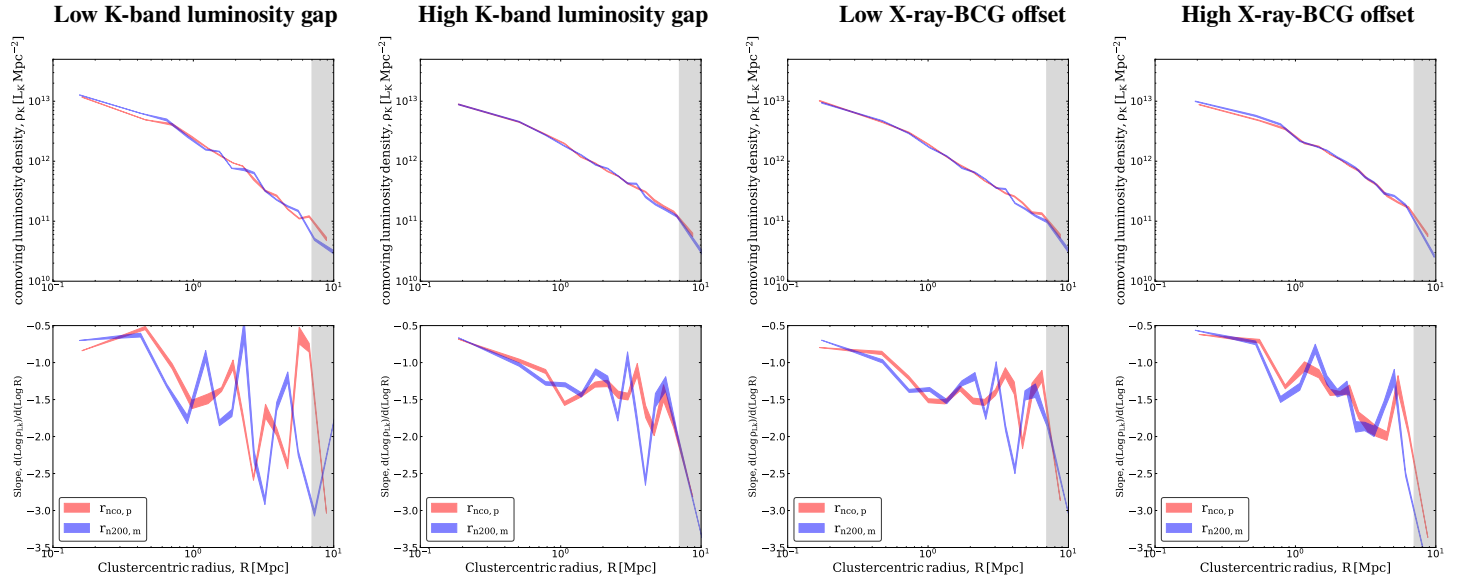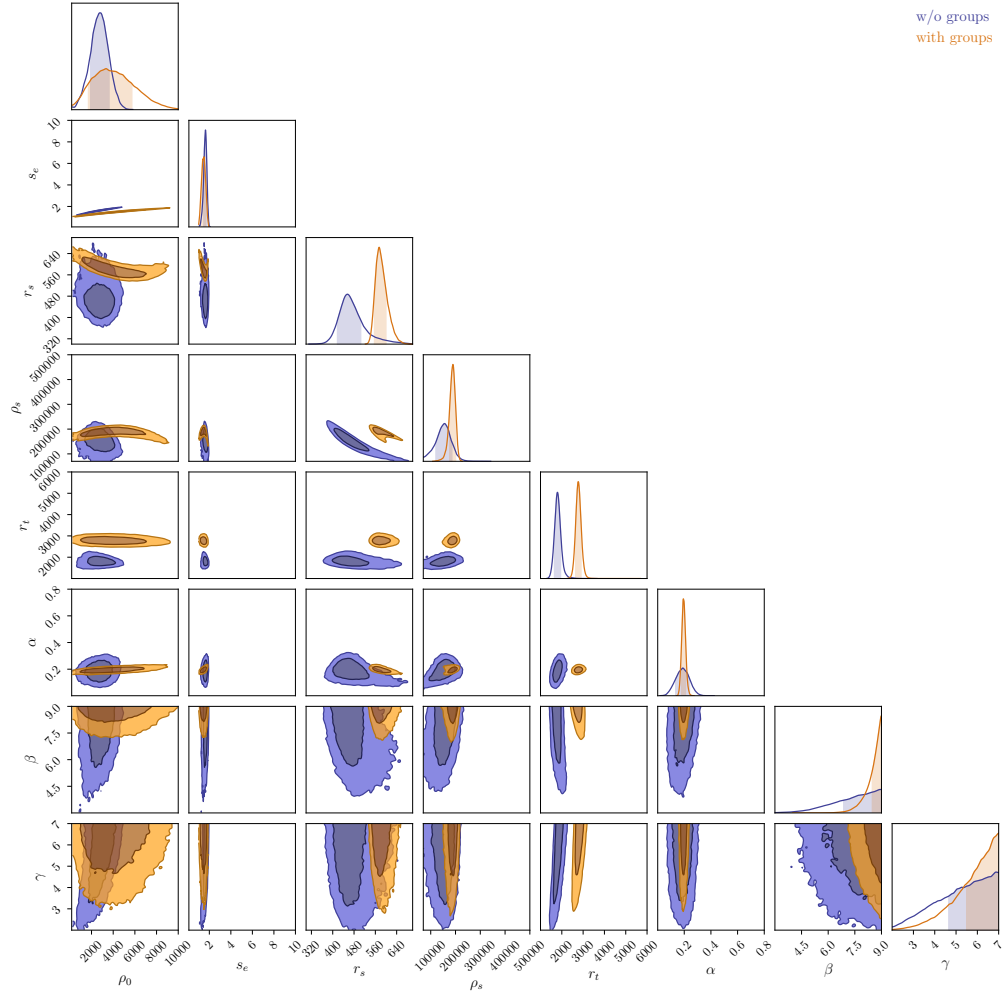
Figure 7. Continued from Figure 6.

Figure 8. Posterior distribution of the parameters of the model fitted to the density profiles of the sample of cluster with and without infalling groups plotted in orange and blue, respectively. Shaded areas in both 1-d and 2-d distributions correspond to 1 σ intervals. The range used in each individual parameter subpanel corresponds to the prior interval.